Shock-less interactions of ablation streams in tungsten wire array z-pinches

G. F. Swadling, S. V. Lebedev, G. N. Hall, F. Suzuki-Vidal, G. Burdiak et al.

Citation: Phys. Plasmas **20**, 062706 (2013); doi: 10.1063/1.4811385
View online: http://dx.doi.org/10.1063/1.4811385
View Table of Contents: http://pop.aip.org/resource/1/PHPAEN/v20/i6
Published by the AIP Publishing LLC.

Shock-less interactions of ablation streams in tungsten wire array z-pinches

G. F. Swadling, S. V. Lebedev, G. N. Hall, F. Suzuki-Vidal, G. Burdiak, A. J. Harvey-Thompson, S. N. Bland, P. De Grouchy, E. Khoory, L. Pickworth, J. Skidmore, and L. Suttle
The Blackett Laboratory, Imperial College, London SW7 2AZ, United Kingdom

(Received 5 April 2013; accepted 13 May 2013; published online 28 June 2013)

Shock-less dynamics were observed during the ablation phase in tungsten wire array experiments carried out on the 1.4 MA, 240 ns MAGPIE generator at Imperial College London. This behaviour contrasts with the shock structures which were seen to dominate in previous experiments on aluminium arrays [Swadling *et al.*, Phys. Plasmas **20**, 022705 (2013)]. In this paper, we present experimental results and make comparisons both with calculations of the expected mean free paths for collisions between the ablation streams and with previously published Thomson scattering measurements of the plasma parameters in these arrays [Harvey-Thompson *et al.*, Phys. Plasmas **19**, 056303 (2012)]. © *2013 AIP Publishing LLC*. [http://dx.doi.org/10.1063/1.4811385]

I. INTRODUCTION

Wire array z-pinch implosions are efficient and powerful sources of soft X-ray radiation, producing peak powers of up to 280 TW[1] and yields of up to 1.8 MJ. They are used extensively as drivers for experiments in fields such as inertial confinement fusion,[2,3] laboratory astrophysics,[4] high energy density physics, and radiation science.[5] An up-to-date review of the physics of these sources was recently published by Haines.[6]

The underlying dynamics of z-pinch implosions have been studied experimentally over a wide range of drive parameters. In general, their evolution can be divided into a sequence of four reasonably distinct phases; initiation, ablation, implosion, and stagnation.[7–9] The ablation phase is by far the longest of the four phases; at 1 MA it has been shown to account for ~80% (Ref. 7) of the total implosion time (the period from current start to the peak of x-ray output) and ~65% at 20 MA.[9] During this phase, the wires are heated and gradually ablate plasma which is accelerated towards the array axis by the J × B (Lorentz) force. The dense wire cores remain stationary until the start of the implosion phase. The ablation phase is responsible for a significant redistribution of the array mass and this redistributed mass sets the initial conditions for the snowplough-like implosion. It is therefore important that we properly understand the physics governing the ablation process.

In our previous paper,[10] we presented the results of experiments investigating the structures formed by the interactions of ablation streams in aluminium wire arrays, diagnosed using an imaging interferometry system aligned end-on to the array. The interferograms captured in these experiments showed that the electron density distributions were dominated by networks of oblique shock fronts, formed by the collisional interactions of neighbouring ablation streams as they converged towards the axis.

In this paper, we focus on the results of tungsten wire array experiments. Tungsten wire arrays are used much more commonly in large scale z-pinch driven experiments and have therefore been investigated in a great deal more detail.[9,11–14] The dynamics observed in the experiments presented in this paper proved to be very different from those observed in the aluminium experiments. The formation of collisional structures was not observed; instead the electron density distributions varied smoothly between the ablation streams and inter-wire gap regions. These observations indicate that the mean free paths (MFPs) for the interactions of the adjacent ablation streams in these arrays are dynamically significant.

It has long been known that tungsten wire arrays should exhibit non-fluid behaviour, especially at early times.[14–16] This paper presents both quantitative and structural data on this behaviour. We present the results of these experiments alongside calculations of the expected collisional mean free paths for these plasmas. These results are then discussed with reference to previously published Thomson scattering measurements of the plasma conditions in these arrays.[17,18]

II. EXPERIMENTAL SETUP

The experiments described in this paper were carried out at Imperial College London using the 1.4 MA, 240 ns rise-time MAGPIE[19] generator. The targets investigated in these experiments were 16 mm diameter cylindrical arrays of between 8 and 128 equally spaced fine tungsten wires. The diameters of the wires used varied depending on the specific wire number of the array, typically falling between 15 and 30 μm. The arrays were purposefully designed to be over-massed in order to suppress the implosion phase, thus minimising the effects of stagnation radiation on the diagnostic suite.

The end-on interferometry system used in these experiments was described in detail in our previous publication.[10] Fig. 1 contains schematics of the layout of this diagnostic and the associated imaging optics. The interferometer is based on a Mach-Zehnder design, with probing beams provided by an Ekspla SL312P, a pulsed, SBS compressed, flash lamp pumped commercial Nd:YAG laser system. Typical pulse durations are ~500 ps, which is sufficiently short to prevent significant blurring when capturing the dynamics of

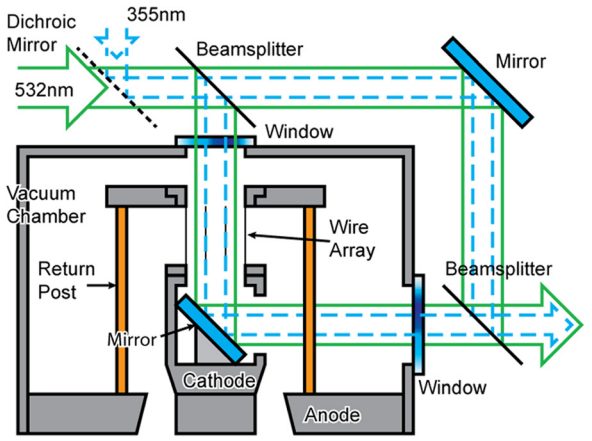

FIG. 1. Schematic side-on view of the apparatus used for end-on probing experiments.

wire array experiments; at an ablation velocity of $\sim 10^7$ cm s^{-1}, we might expect plasma motion of $\sim 50\,\mu$m over this period. The effective resolution of the analysed data is limited chiefly by the spacing of the fringes. This spacing introduces an error in the resulting electron density maps due to the linear interpolation technique used. The fringe spacing used in these experiments is a compromise between this resolution and the ability to resolve separate fringes in the regions of strong electron density gradients. Overall, the smallest structures we are able to resolve are on the scale of $\sim 100\,\mu$m. Two different wavelengths are used in the interferometer, the 2nd (532 nm) and 3rd (355 nm) harmonics of the Nd:YAG fundamental (1064 nm). The design of the laser optics allows the time delay between these two frames to be varied between 0 and 24 ns. Typically, the 355 nm frame is fielded at later times than the 532 nm frame, as the 355 nm probe wavelength is less sensitive to gradients in the plasma electron density and thus better at penetrating higher density plasmas.

The interferograms are captured using standard Canon DSLR cameras (model numbers 450D and 550D). The shutters of these cameras are held open for the entire duration of the experiment; the temporal resolution of the imaging system is therefore set by the laser pulse duration. The visible-spectrum band-pass filter was removed from one of the cameras' CCD in order to allow it to capture images at 355 nm (near UV). In normal photography, this filter protects the CCD from the unwanted effects of IR and UV radiations. Fig. 2 shows an example of interferometry data captured in a 32 wire tungsten array experiment.

Analysis was carried out using the method discussed in our previous publications.[10,20] The positions of the fringe minima were traced for both the reference and experimental interferograms and this information was then used to construct interpolated maps of the relative fringe shift for each. The fringe shift produced by the plasma was then obtained by subtracting the reference fringe map from the experimental one. This map was converted into an areal electron density map using a calibration factor calculated using the equations for the free electron refractive index, and finally, the axially averaged density was found by dividing this areal density by the length of the array.

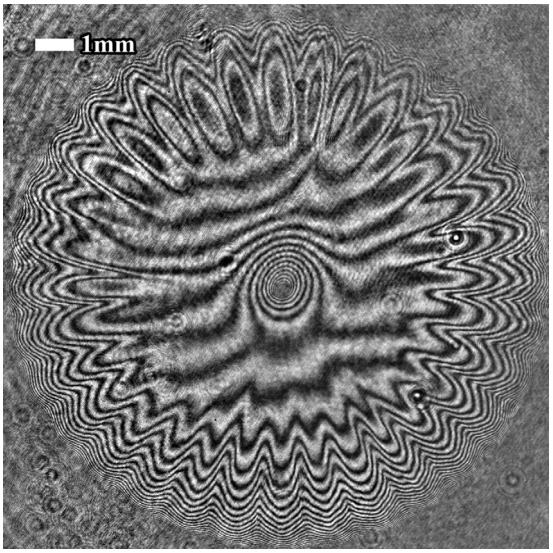

FIG. 2. An example of a 355 nm end-on interferogram captured during a 32 wire tungsten wire array experiment at 140 ns. The results of the analysis of this image are shown in Fig. 4.

It is important to emphasise the axially averaged nature of the resulting density map. Previous work has shown that the ablation rate along the length of each wire core is modulated at a well-defined wavelength ($\lambda \sim 0.25$ mm for W),[21] and that this leads to a modulation of the ablation stream density (typical amplitude $\sim$50%).[22] Apart from these regular modulations in density, the overall dynamics along the array length are uniform, and thus, our axial average should give a good handle on the overall array dynamics.

Some changes have been made to the method used to interpolate the fringe maps since our last publication[10] on this topic. Previously, we used a linear Delaunay triangulation method to interpolate the fringe shift map from the traced fringe positions. This method is best suited to spatially scattered datasets and is certainly not ideal for interpolating the contour-like datasets produced by fringe tracing. It produces artefacts in the interpolated data, particularly in regions where fringe shifts are small. A modified triangulation method was developed which better fits the contour–like fringe data. This method was successful in removing the majority of the artefacts and led to a significant improvement in the reliability of the resulting data. Although this method represents an improvement over the previous one, this change does not impact the validity of our previous work,[10] as it does not change the overall geometry of the shock structure. For comparison, Fig. 3(a) shows the results of this improved technique as applied to our previously published 32 wire aluminium array data.[10]

III. REVIEW OF ALUMINIUM EXPERIMENTS

In order to put the results described in this paper into proper context, we shall briefly review the results of our previous experiments[10] investigating the ablation phase of aluminium wire arrays.

The interactions of adjacent ablation streams in aluminium wire arrays are dominated by the formation of oblique

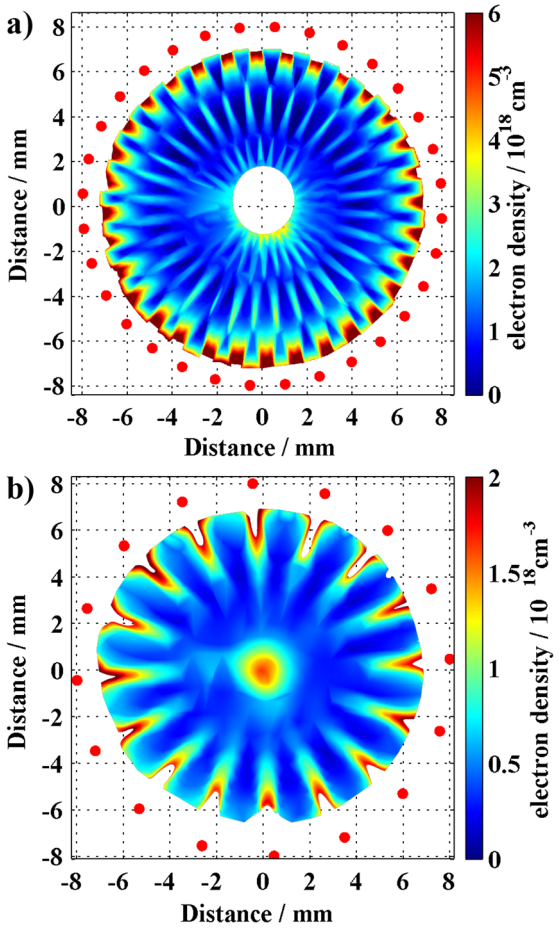

FIG. 3. Electron density distributions for aluminium arrays. Red spots mark initial wire positions (a) 32 wire array at 140 ns. (b) 16 wire array at 107 ns. Collisional structures are yet to form.

shock structures. The structure of these shocks can be seen most clearly in the data from the 32 wire array experiments, an example of which is shown in Fig. 3(a). Here, a series of oblique shocks forms a regular diamond-like pattern extending towards the array axis. Radial convergence of the array mass appears to be mediated across these shock fronts, with the density of the flows approximately doubling across each. The oblique shock structures formed by the interactions of the aluminium ablation streams are reproduced well by GORGON[23,24] 3D MHD numerical modelling.[10]

The electron density distributions produced by 16 wire aluminium arrays were characterised by similar collisional structures, although these structures were more complex than those observed in the 32 wire data. The major difference in this case is that the azimuthal separation of the wire cores are doubled, which also doubles the approach velocities of the adjacent streams. The majority of the data captured in the 16 wire experiments contained these shock structures,[10] however, in one experiment an interferogram captured at a very early time (107 ns) showed evidence of a different interaction regime. Fig. 3(b) shows the electron density map produced from this interferogram. The image shows no evidence of collisional structures; no shocks have formed in the interwire regions, and there is no azimuthal structuring of the precursor region on axis. This smooth structure was not observed in interferograms captured at similar times for 32 wire aluminium arrays.

The equations describing the collisional mean free paths[25] of the interacting streams provide a possible explanation for this change of dynamics. The mean free path scales quadratically with the kinetic energy of the collision and linearly with their particle density. The increased approach velocity of the ablation streams in the 16 wire case could bring the plasma into a non-collisional regime at early times. An image captured 24 ns later in the same experiment, when the density of the ablation streams had increased by approximately an order of magnitude, clearly showed the expected collisional features. Section V A includes further calculations and discussions of the mean free paths for aluminium arrays.

The long mean free path dynamics hinted at in the aluminium data are much more pronounced when we change the wire material to tungsten. Analysis of the structures observed in this regime form the main topic of interest for the remainder of this paper.

IV. TUNGSTEN ARRAY EXPERIMENTAL RESULTS

Figs. 3(a) and 4(a) show typical examples of the electron density distributions obtained from interferograms captured during 32 wire aluminium and tungsten experiments, respectively. The two interferograms were captured at similar times, in experiments with similar current drives; the only change made between the two experiments was the wire material. The difference in flow dynamics is immediately obvious; the tungsten data appears smooth, in contrast to the shock structures observed in the aluminium data. The transition between the ablation streams and the interwire gaps in the tungsten data is gradual and continuous, with no evidence of discontinuities. In the aluminium data (Fig. 3(a)), the regions of highest density at the edge of the field of view corresponded to the azimuthal positions of the inter-wire gaps; these high density regions are produced by the collision of material ablated directly from the wire cores[10] and are bounded on either side by shock fronts. In the tungsten array data, the regions of highest density at the perimeter of the field of view correspond to plasma flowing directly from the initial wire positions.

As we follow the flow of ablation plasma towards the axis in Fig. 4(a), we see that the contrast ratio between the ablation streams and the inter-wire gaps gradually decreases, until there appears to be almost no azimuthal structure to the electron density in the region directly surrounding the axis. Fig. 4(b) shows a pair of azimuthally separated radial density profiles taken though Fig. 4(a). The paths of these profiles are marked in plot Fig. 4(a) by arrows at the edge of the field of view; the black line corresponds to the azimuthal position of an ablation stream flowing directly from a wire core, while the red line passes down the middle of an adjacent interwire gap. The two profiles illustrate how the density modulation produced by the discrete ablation streams is smoothed out as the streams approach the axis. At large radius, the two profiles show a significant contrast in density between the ablation stream and the inter-wire gap; however,

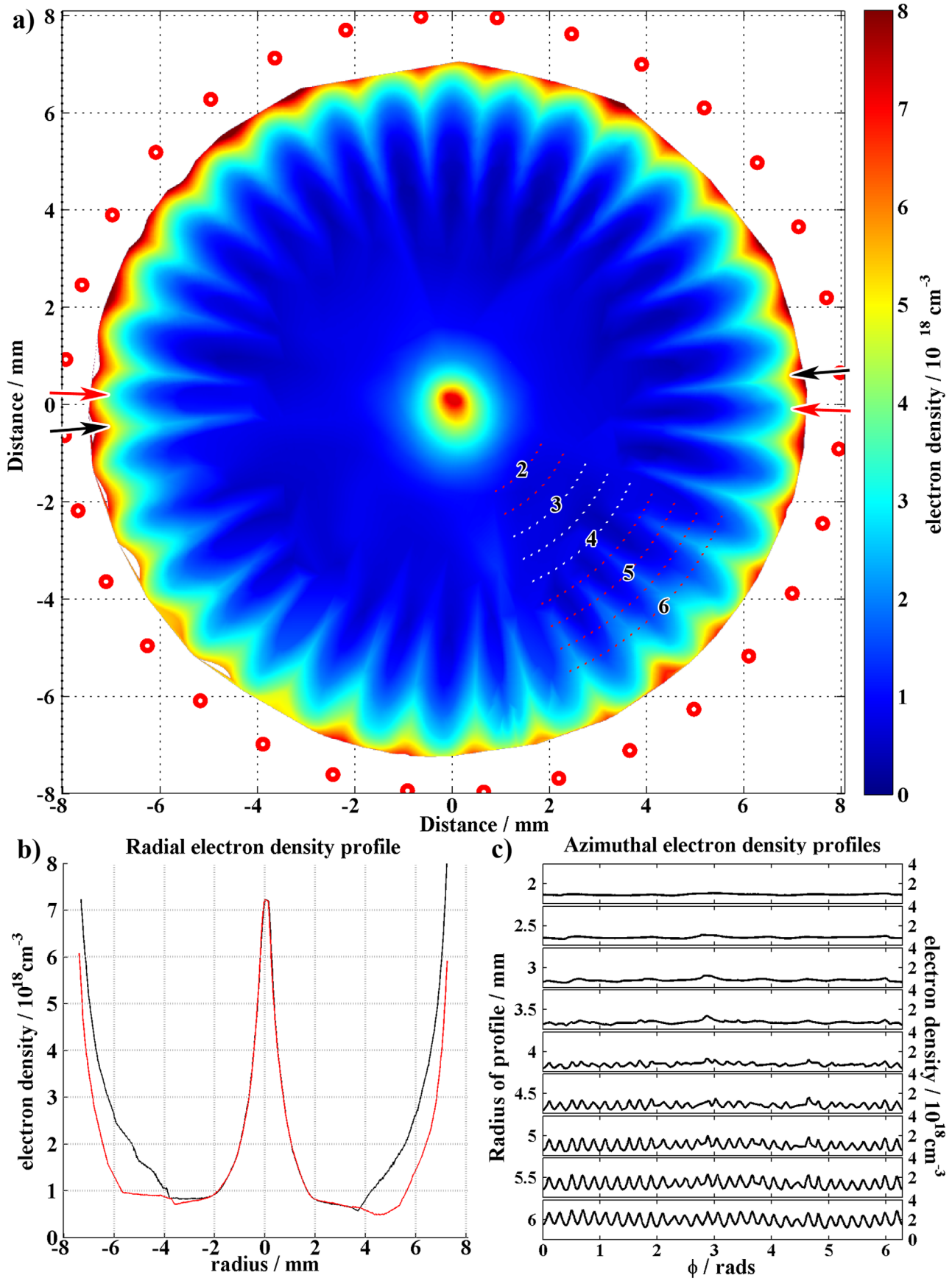

FIG. 4. (a) Electron density map of a 32 wire W array at 140 ns. This data was extracted from the interferogram shown in Fig. 2. Red dots mark the initial wire positions. (b) Radial line profile taken through the data in (a). The solid black line shows a profile along the centre of an ablation stream, while the red (grey) line shows the profile along the centre of the inter-wire gap. The positions of these line profiles are indicated by arrows on (a). (c) Azimuthal line profiles. The radius at which each profile was taken is indicated by the arcs in (a). The profiles were taken about the full azimuth. Each arc is marked with its radius in mm.

as the streams approach a radius of ~3–4 mm, the densities of the two profiles rapidly converge, and inside r ~ 3 mm the two profiles appear to match almost exactly, leaving no evidence of any azimuthal structure to the density distribution.

The process of azimuthal smoothing is further illustrated in Fig. 4(c). This figure shows a series of density profiles taken about the azimuth ($\theta = 0$-2π) of the array, over a range of radii (r = 2–6 mm), at intervals of 0.5 mm. Portions of the paths corresponding to these profiles are indicated by the dotted arcs overlaid on Fig. 4(a); those which correspond to the range r = 3–4 mm, over which the majority of the smoothing appears to take place, have been marked in white. This figure clearly shows that the process of smoothing occurs uniformly at the same radius in all azimuthal directions about the array axis. It also illustrates the speed of the process. Between r = 6 and r = 4.5 mm, any changes to the contrast ratio are quite minor; however, between r = 4 and r = 3, the change is dramatic. Over this range, the regular azimuthal structure almost completely disappears.

Experiments were carried out using 8 wire arrays in order to further investigate this azimuthal smoothing process. The main motivation for using 8 wire arrays was that the azimuthal separation of the wires in these arrays is much larger than in 32 wire case. This means there is a significant increase in the size of the interwire gaps.

Fig. 5(a) shows a typical example of the electron density distributions seen in the 8 wire results. Fig. 5(b) shows a series of azimuthal electron density profiles taken through this data, similar to those shown in Fig. 4(c). At large radius the profiles of the ablation streams are sharp and well defined; the regions corresponding to the interwire gaps are almost completely clear of plasma. The profiles of the ablation streams at large radius are so sharp that they obscure the probing beam. This is most likely due to the sharp gradients deflecting the probing radiation out of the collection cone of the imaging system, rather than because of any attenuation in the plasma. The ring of apparent high density seen around the circumference of the field of view in this plot is caused by high density electrode plasma expanding from the wire mounting rings. This plasma does not extend along the length of the array and is not dynamically important.

Again in this data, we see that as the streams approach the axis there is a rapid transition to a smooth, azimuthally isotropic distribution of the electron density about the axis. In this case, the process appears to take place over a range of radii r ~ 2–3 mm; this range of profiles is marked in white on Fig. 5(a). Although this radius is smaller than the radius at which this effect was observed in the 32 wire data, it is not as small as we might expect given the initially narrow and focused profiles of the ablation streams.

The azimuthal smoothing was further investigated by taking measurements of the radius at which the electron density became smoothed over a range of imaging times and wire numbers; the results are plotted in Fig. 6. In each case, the smoothing radius was measured by comparing radial density profiles like those shown in Fig. 4(b). The point at which the two lines converged was selected as the smoothing radius. In some cases, two separately timed interferograms were captured in the same experiment; in these cases, the

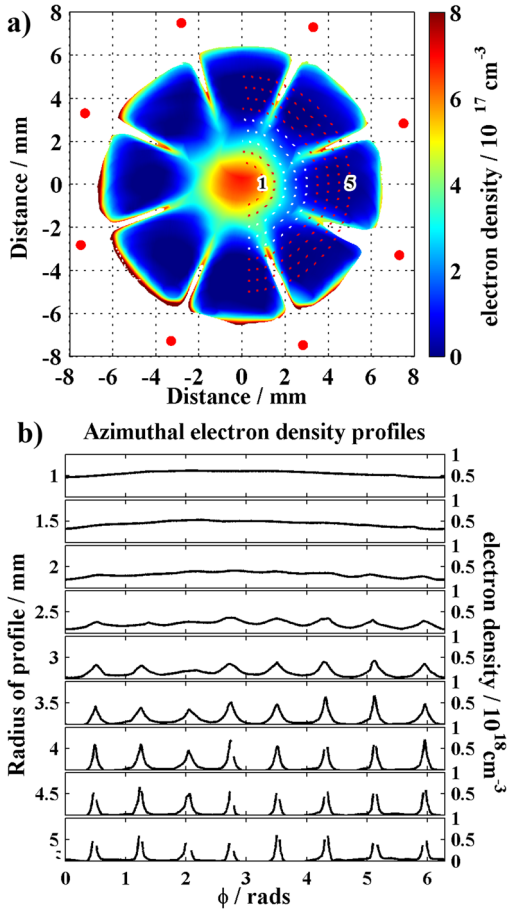

FIG. 5. (a) Electron density distribution for an 8 wire tungsten array at 128 ns. Initial positions of the wire cores are marked with red spots. (b) Azimuthal line profiles taken from the data in (a). The radius of each profile is indicated in (a) by a series of labelled arcs. The profiles are taken about the full azimuth of the array.

earlier point corresponded to the 532 nm interferogram, while the later point is measured from the 355 nm interferogram. Inspection of Fig. 6 reveals two broad trends. First, for each fixed wire number, we see that the radius at which the profiles become azimuthally isotropic tends to decrease over time. In particular, it should be noted that this is always the case when comparing two frames captured in the same experiment and that these all show the same approximate rate of radial convergence ($\delta r/\delta t \sim 3.3$–$4 \times 10^4\,\mathrm{ms}^{-1}$). The mismatch in timing of this convergence in the two 32 wire shots shown in Fig. 6 is most likely the result of current variation between the two shots. Second, we see that increasing the wire number of the array tends to lead to a larger radius at which the profile becomes azimuthally smoothed. This is to be expected, as the separation of the ablation streams at any given radius increases with decreasing wire number.

The shock-less behaviour described above appears to be present even in arrays with very large wire numbers, as illustrated in Fig. 7, which shows an interferogram and the corresponding density map from a 128 wire tungsten array experiment.

In Sec. V, we will present calculations of the collisional mean free paths associated with the interactions of adjacent ablation streams and discuss the plasma conditions in the

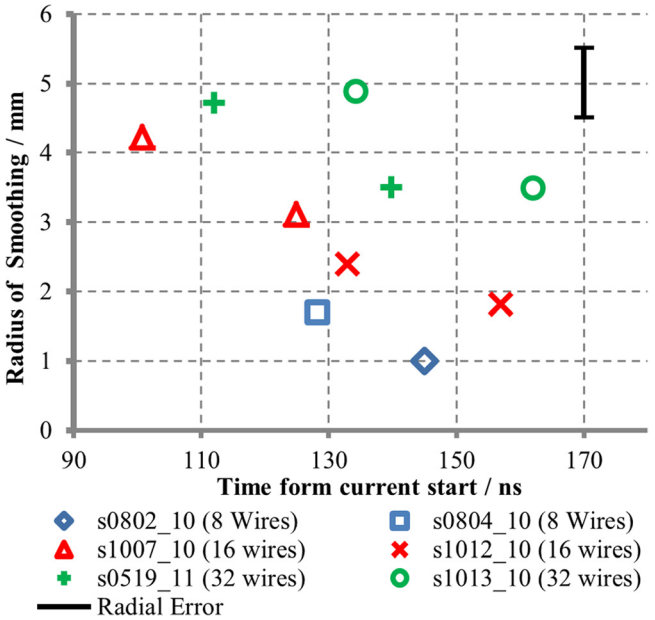

FIG. 6. This plot shows the radius at which the electron density profiles of various tungsten arrays were measured to become azimuthally isotropic. These points were measured by comparing on and off stream radial profiles like those shown in Fig. 4(b). In the case where two points are shown for a single experiment, these correspond to the two separately timed laser imaging frames.

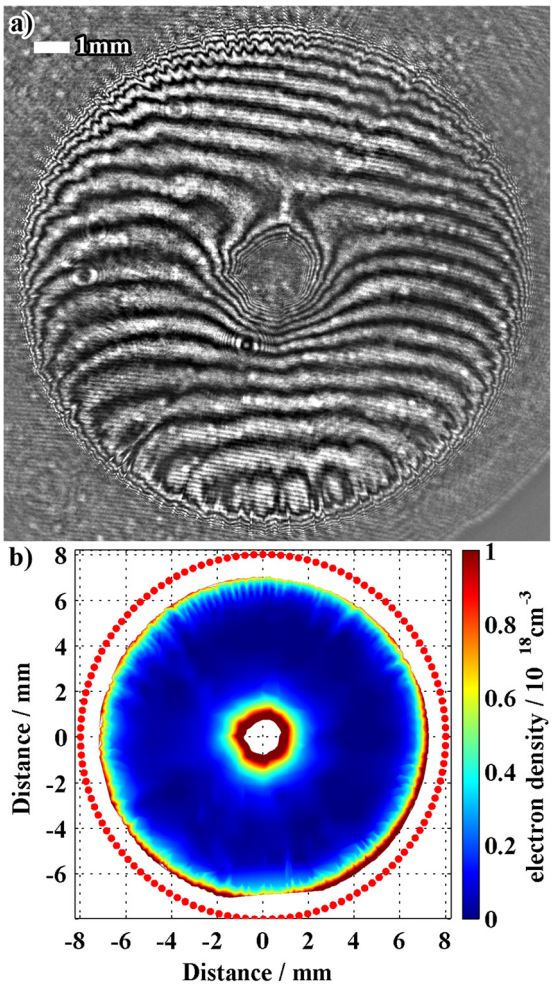

FIG. 7. 128 tungsten wire array data captured at 130 ns. (a) Raw interferogram. (b) Analysed data. No shocks structures are evident.

streams which are required in order to explain the absence of collisional structures in the tungsten interferometry data.

V. INTER-STREAM MEAN FREE PATH CALCULATIONS

The absence of shock structures in the tungsten wire array data indicates that the scale length for the collisional interactions between the adjacent ablation streams must be at least comparable to the widths of the streams themselves. In order to further investigate these dynamics, we will require the formulae for the Coulomb collision frequencies.[25,26] The Appendix includes a brief overview to these equations and their scalings. In order to calculate the expected MFPs for collisions between adjacent ablation streams, we must first recast the problem to fit the model. In the model, interactions take place between test particles traveling with some initial velocity and a thermal field of scattering particles. The collision of a pair of ablation streams must therefore be modelled in the rest frame of one of them, and the velocity of the test particles is then equal to the approach velocity of the two streams. The radial flow velocity of the ablation streams in wire arrays has been measured in previously published Thomson scattering experiments,[17,18] and appears to be reasonably insensitive to the number of wires and the wire material. In all cases, the measured velocity was observed to increase as the stream approached the axis. For 8 mm radius aluminium arrays, the measured velocity varied from $0.5–1.2 \times 10^5\,\mathrm{ms}^{-1}$ over a radial range of r = 7–1 mm, whilst for the tungsten arrays it varied between $0.6–1 \times 10^5\,\mathrm{ms}^{-1}$. The similarity of the tungsten and aluminium ablation velocities (v_{Abl}) is important, as the collisional MFP scales quadratically with the kinetic energy of the colliding particles ($\lambda_{mfp} \propto E^2$). If $\vec{v}_W \sim \vec{v}_{Al}$, then, since the ion kinetic energy is proportional to the atomic mass (A), $E_W \sim (A_W/A_{Al})E_{Al}$, which, ignoring any other factors, should result in an increase in the expected MFP by a factor of $\lambda_W/\lambda_{Al} = (A_W/A_{Al})^2 \sim 46$. For the calculations presented below, we used the velocity seen at r = 3–4 mm, $v_{abl} \sim 10^7\,\mathrm{cm\,s}^{-1}$.

Assuming that the ablation streams flow radially and that collisions between the streams occur due to radial convergence, the approach velocity of the two streams can be calculated based on the geometry of the wire array. This geometry is shown schematically in Fig. 8 and leads to the following expression for the approach velocity in terms of the wire number (N_w):

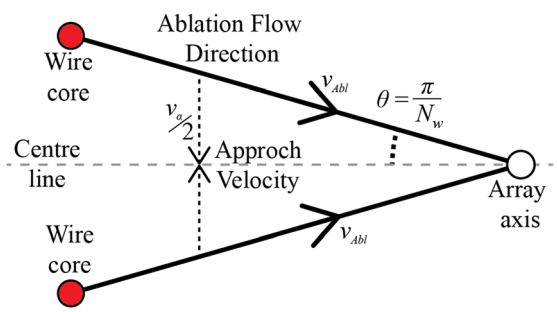

FIG. 8. Diagram of the collisional geometry for a pair of adjacent, radially converging ablation streams. The resulting approach velocity is given by Eq. (1).

$$v_a(N_w) = 2v_{Abl}\sin\left(\frac{\pi}{N_w}\right). \quad (1)$$

For an 8 wire array, $v_a = 0.76 \times v_{Abl}$; for a 16 wire array, $v_a = 0.39 \times v_{Abl}$; and for a 32 wire array, $v_a = 0.20 \times v_{Abl}$. It should be noted that these estimates of the approach velocities ignore the possibility of any divergence of the ablation stream flow vectors. Equation (1) corresponds directly to the situation depicted in Fig. 8; it gives the approach velocity corresponding to a pair of flows launched from the centres of two neighbouring wire cores directly towards the array axis, such that they will collide on axis. This calculation produces the smallest possible approach velocity. In the case that the streams are divergent, collisions between the streams will occur along the centre line shown in Fig. 8, resulting in a larger angle of incidence between the flows, which will in turn result in an increased effective approach velocity. In aluminium arrays, we have seen evidence of strongly divergent flows of plasma directly from the wire cores, leading to the formation of shock structures at very large radius. Since the collisional MFP scales as v_a^4, calculations using the velocity given by Eq. (1) will correspond to a lower limit for the MFP.

The two streams are assumed to be identical, and thus, the particles in each are treated identically. The charge of the ions is written in terms of electron charge (e_e) and the average ionization ($\bar{Z}$), $e_i = \bar{Z}e_e$. The electron density of the streams was taken from the end-on interferometry data. The ion density was then found by dividing this electron density by the average ionisation, $n_i = n_e/\bar{Z}$. Substituting these two relations into the equations for the slowing down MFP ($l_s^{\alpha\backslash\beta}$, Eq. (A3), Appendix) results in expressions for MFP in terms of the electron density (n_e) and average ionisation ($\bar{Z}$) of the plasma. First, we find the expression for the ion-ion MFP,

$$l_s^{i\backslash i} = \frac{1}{2\psi(x^{i\backslash i})\lambda_{ii}}\frac{(m_i V_i^2/2\ )^2}{\pi n_i \bar{Z}^3 e_e^4}, \quad (2)$$

and second, for the ion-electron MFP,

$$l_s^{i\backslash e} = \frac{1}{\left(1+\frac{m_i}{m_e}\right)\psi(x^{i\backslash e})\lambda_{ie}}\frac{(m_i V_i^2/2\ )^2}{\pi n_e \bar{Z}^2 e_e^4}. \quad (3)$$

Inspection of these equations reveals the sensitivity of the mean-free path to both the average ionisation of the plasma and the approach velocity (v_a). Functions $\psi(x^{i\backslash i})$ and $\psi(x^{i\backslash e})$ are the "velocity potentials" for the two types of interaction; this is a normalised parameter which is dependent on the temperature of the plasmas and tends to decrease as the temperature increases. Functions λ_{ie} and λ_{ii} are the coulomb logarithms for these interactions. The equations used to calculate these parameters are discussed in the Appendix along with a short discussion of their physical interpretation.

An accurate estimate of the average ionisation ($\bar{Z}$) of these high atomic number plasmas is challenging. Direct experimental measurements of this parameter have not yet been made in our experiments, and the densities of the regions of interest for our calculations are low enough that we cannot really rely on the results of calculations based on the assumptions of local thermodynamic equilibrium (LTE). The methods used in each case are therefore discussed in more detail in their respective sections. The electron temperatures of the plasmas are also not well known. The electron temperature of the ablation streams has been measured using Thomson scattering in only a very limited number of experiments, and in those cases the lack of spectral resolution meant that the results could only be treated as upper limits for this parameter, $\bar{Z}T_e < 100$ eV.[18] For our calculations, we relied on the results of MHD simulations using the GORGON code, which indicate that temperatures in these ablation flows should be around $T_e \sim 10$–20 eV.[27]

Calculations of the slowing down MFP were carried out over a range of plasma parameters. In particular, we investigated the effects of changes in electron density (n_e) and ionisation state ($\bar{Z}$) of the plasma. These calculations revealed that over the range of plasma parameters considered in this paper the MFPs associated with the ion-ion interactions were dominant, being at least an order of magnitude shorter than those corresponding to the ion-electron interactions. As a result, for the sake of clarity, the ion-electron MFPs have not been included in the plots.

A. Calculations for aluminium arrays

Calculations of the collisional MFPs for aluminium arrays were carried out in order to provide a point of comparison with the tungsten results. For the aluminium array calculations, we estimated the ionisation state of the plasma based on polynomial fits taken from Post *et al.*[28] These fits are based on calculations using an average ion model in which the plasma is treated as optically thin and the populations are determined by balancing the rate of collisional ionisation against the rates of dielectronic, radiative, and three-body (collisional) recombination. While it is not strictly applicable to the regime of this problem, it was felt that this model would provide a more accurate result than that obtained by solving the Saha rate equations. For the following calculations, we used a plasma temperature of 20 eV and a $\bar{Z}$ of 3.5 (this is probably the lower boundary of possible $\bar{Z}$). For the sake of simplicity, we assumed that the plasma has had time to equilibrate and therefore have modelled the plasma with a single temperature.

Fig. 9 shows plots of the variation of the ion-ion MFP (Eq. (2)) with electron density for aluminium arrays with 16 and 32 wires. The calculations were performed using $\bar{Z} = 3.5$; changes to this parameter will scale these plots as $\bar{Z}^{-3}$. The plot can be used to explain the changes in collisional dynamics seen at early times in the 16 wire data.[10] The lowest inter-stream electron density measured in the 32 wire data was $\sim 10^{17}\,\mathrm{cm}^{-3}$, which, as Fig. 9 shows, corresponds to a MFP of $\sim 100\,\mu$m. Since shocks were observed in this experiment, we can use this value as an upper bound for the MFP required to trigger shock formation. Changing to a 16 wire array, the effective approach velocity for collisions between the neighbouring streams doubles (see Eq. (1)), resulting in a $\sim$16 fold increase in the ion-ion MFP due to the v_{ap}^4 scaling (Eq. (2)). The MFP for a 16 wire array

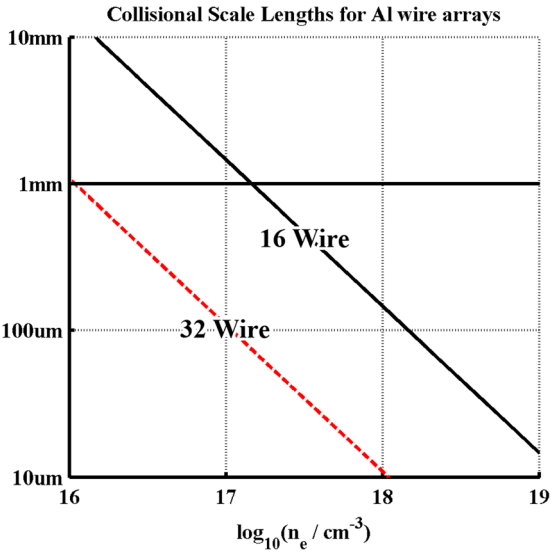

FIG. 9. Ion-ion mean free paths for inter-stream collisions of 16 and 32 wire aluminium arrays as they vary with the electron density of the plasma.

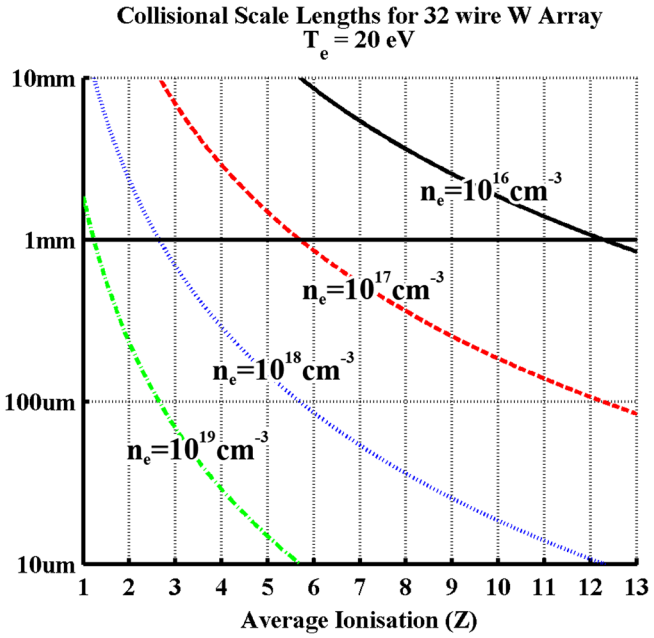

FIG. 10. Ion-ion mean free paths ($l_s^{i\,i}$) for collisions of adjacent ablation streams in a 32 wire tungsten array with varying $\bar{Z}$ and n_e.

with $n_e = 10^{17}\,\mathrm{cm}^{-3}$ is therefore $\sim$1 mm, an order of magnitude larger than the upper bound for the formation of shocks that we took from the 32 wire data, and comparable to the width of the ablation streams themselves. This explains the absence of shock structures in the data captured at early times for 16 wire arrays (see Fig. 3(b)). As the electron density increases towards $\sim 10^{18}\,\mathrm{cm}^{-3}$, Fig. 9 shows that the MFP should approach $\sim 100\,\mu$m, which is consistent with our observations of shock formation at later times in 16 wire arrays.[10]

B. Calculations for tungsten arrays

The Post model,[28] which we used in Sec. V A to estimate $\bar{Z}$ for aluminium, cannot be applied to our tungsten calculations as the expected plasma electron temperature (T_e) lies well outside the range of the tungsten polynomial fit ($T_{min} = 100\,\mathrm{eV}$).[28] An alternative approach to estimating the ionisation state of the tungsten plasma is to solve the Saha rate equations. For a tungsten plasma with an electron density of $10^{18}\,\mathrm{cm}^{-3}$ and a temperature range of 10–20 eV (Ref. 27), this method predicts $\bar{Z} \sim 7.2$–12.5. It should be noted however that the low density and temperature of the ablation streams means that this LTE model is likely to overestimate the ionisation state. Inspection of the ionisation potentials of tungsten[29] reveals that the ionisation potential required to take W ions from $\bar{Z} = 12 \rightarrow 13$ is 258 eV, making the top end of the estimate range seem particularly unlikely. Due to the difficulties in accurately estimating the ionisation state of the plasma, it was decided to make plots of the variation of the MFP over a range of $\bar{Z}$. The results of these calculations will be compared to the experimental results in order to estimate the range of $\bar{Z}$ consistent with the data.

Fig. 10 contains plots of the ion-ion MFPs for 32 wire tungsten arrays, calculated using Eq.(2). The MFPs are plotted against $\bar{Z}$ for a range of electron densities. In general the MFPs calculated for tungsten arrays were much longer than those calculated for aluminium arrays, consistent with our experimental observations. For $n_e < 10^{17}\,\mathrm{cm}^{-3}$, the tungsten MFPs are larger than 100 μm over almost the full range of possible $\bar{Z}$ (In our earlier analysis of the aluminium data, we found that a MFP of $\sim 100\,\mu$m was the longest for which shock formation was observed). As the electron density of the plasma increases, the MFP decreases significantly. The highest electron density observed in the inter-stream regions of the tungsten arrays, measured at the latest time possible using our current experimental setup, was $n_e \sim 10^{18}\,\mathrm{cm}^{-3}$. Our observation of shock-less dynamics in the interferometry data at this time allows us to infer an upper limit on the possible ionisation state of the tungsten plasma. Based on our upper limit of $\sim 100\,\mu$m for shock formation, we find the upper limit for the ionisation state to be $\bar{Z} < 6$. Even a relatively modest increase in the $\bar{Z}$ above this level will result in a significant decrease in the MFP, due to the $\bar{Z}^{-3}$ scaling in Eq. (2). A $\bar{Z} < 6$ in a plasma with $\sim 10^{18}\,\mathrm{cm}^{-3}$ corresponds to a temperature of $T_e < 6\,\mathrm{eV}$ in the ablation streams, based on a Saha rate equation solution.

If we assume that the ionisation state in the streams is at the very least $\bar{Z} > 3$, then Fig. 10 suggests that we might expect shocks to form between the tungsten ablation streams as the electron density in interwire gaps approaches $n_e \sim 10^{19}\,\mathrm{cm}^{-3}$. The latest probing time possible in these experiments was set by the lifetime of the mirror mounted in the cathode (see Fig. 1). The intensity of the radiation pulse produced during the collapse of the precursor column[15] was enough to destroy the reflectivity of this mirror, which led to a practical limit for the probing time of $\sim$140 ns. It is hoped that changes to the experimental hardware may allow us to overcome this limitation in future experiments, allowing us to take measurements at later times and higher densities, and perhaps to observe the onset of collisionality.

VI. DISCUSSION OF AZIMUTHAL SMOOTHING

Although no shock structures were observed in the tungsten data, we did see a change in the azimuthal structure of the ablation streams as they approached the axis of the array. The data in Sec. IV showed that the electron density distribution in tungsten arrays undergoes a process of azimuthal smoothing as the streams approach this axis. One could consider the following four possible explanations for this phenomenon:

First, the apparent azimuthal smoothing of the electron density profile could be the result of the superposition (overlapping) of the individual density profiles corresponding to each of the ablation streams. This explanation requires that the ablation streams are entirely non-collisional. These streams converge radially towards the array axis, while undergoing some degree of thermal expansion. As they approach the array axis, their separation will decrease, whilst their width will tend to increase. From an end-on view, at a sufficiently small radius the superposition of the individual profiles might appear as an azimuthally isotropic distribution.

Second, we might be able to explain this phenomenon as being the result of medium-scale scattering interactions between the ablation streams. The onset of this scattering process could be triggered by some change in the properties of the plasma as it propagates towards the axis, such as changes in the temperature and/or ionisation state. While no shocks are observed in the data, this does not mean that collisional interactions between the ablation streams are completely absent. Long mean free path interactions could result in a scattering of the velocity distribution of the ablation stream, and this in turn could produce the azimuthally smoothed density profile seen on axis. Since no shock interactions were observed in the experimental data, we should still expect the mean free paths for the inter-stream interactions to be at least comparable to the widths of the ablation streams.

The third possible explanation is that some form of magnetic effect is responsible. It is possible that the collimation of the ablation streams observed at large radius is not simply the result of high Mach numbers in these flows but is also due to the presence of a magnetic confining force, produced by current which is advected towards the axis in the ablation streams. Similar mechanisms have been suggested in order to explain the apparent ablation stream focusing seen in data from cylindrical wire array experiments diagnosed using an axial x-pinch backlighter[30] and for the axial confinement of ablation stream observed in experiments on coiled wire arrays.[31] This magnetic field would provide an additional force which would act to tamp the thermal expansion of the streams. As the streams converge on axis, their separation will decrease, and the current they carry will resistively diffuse outwards. At some point the tamping force will be lost, allowing the streams to expand thermally, and producing the observed distribution. It should however be noted that Thomson scattering measurements have shown that the ion temperature is quite low ($T_i \sim 10\,\text{eV}$) at large radius,[17,18] supporting the view that the streams are at least initially characterised by a high Mach number.

A fourth explanation for the observed smoothing is that it may be the result of some form of heating of the ablation streams. Thomson scattering measurements have demonstrated that at the times relevant to our interferometry measurements, the ion temperature on axis is very high ($T_i \sim$ 3-5 keV within 1 mm of the axis).[17,18] If this heat was to be transferred into the ablation streams, the increase in the temperature of the streams could drive increased thermal expansion, causing the stream to diverge faster. An increased electron temperature in the streams would also drive an increase in the average ionisation state of the plasma, which in turn would lead to a decrease in the collisional mean free paths, and thus stronger scattering between adjacent streams. The increased $\bar{Z}$ of the plasma will however also result in increased radiative cooling, which may act to limit this effect.

The observation of azimuthal smoothing in 8 wire arrays as well as 32 wire arrays suggests that this effect is not the result of the superposition of non-collisional stream profiles. The initially narrow profile and low expansion rate of the 8 wire ablation streams, together with the rapid onset of smoothing, indicate that it must instead be caused by some form of physical interaction between the streams. This interpretation is further supported by previously published Thomson scattering measurements in 8 wire experiments, which showed an absence of the four-peak scattering spectrum, which would be expected on axis if the streams were fully non-collisional.[18]

As discussed in Sec. IV B, a lower limit for the mean free path in the smoothing region, $l_s > 100\,\mu\text{m}$, can be set based on the mean free paths calculated for aluminium arrays in which shock formation was observed (see Sec. V A). For a mean free path shorter than this, we would expect to observe the onset of shock formation. Fig. 4(a) shows that the smoothing region remains shock-less up to at least an electron density of $\sim 10^{18}\,\text{cm}^{-3}$. Fig. 10 shows that these parameters imply an upper limit for the average ionisation of the tungsten plasma of $\bar{Z} < 6$. Assuming the smoothing process is the result of heating, we can calculate the expected temperatures required in the streams. The plasma thermal expansion rate is given by the following expression:

$$v_{ex} = \sqrt{v_{T_i}^2 + C_s^2} = \sqrt{\frac{kT_i}{m_i} + \frac{\gamma Z k T_e}{m_i}}\,, \tag{4}$$

where v_{T_i} is the ion thermal velocity (the result of ion pressure) and C_s is the ion sound speed (driven by the electron pressure). For these calculations, we roughly estimated the effective Mach number ($M = v_{flow}/v_{ex}$) in the smoothing region as $M = 2$–3 based on the expansion rate seen in the 8 wire data in Fig. 5(a), and we used the estimate for the flow velocity given in Sec. V ($v_{flow} \sim 10^7$ cm s^{-1}). As the two terms in the expression for the expansion velocity (Eq. (4)) are independent, we may treat them separately.

Assuming the expansion is dominated by the electron pressure ($v_{ex} \to C_s$), the equations indicate that the plasma must have $\bar{Z}T_e \sim 1500$–$3500\,\text{eV}$, which would correspond to a range of electron temperature $T_e \sim 260$–$600\,\text{eV}$ ($\bar{Z} < 6$). This range is very high. Using the Saha rate solution, we get a

corresponding range $\bar{Z} \sim 16$–50, clearly inconsistent with our limit of $\bar{Z} < 6$, which as we have already shown corresponds to an electron temperature of $T_e < 6\,\text{eV}$.

If instead it is assumed that the expansion rate is dominated by the ion thermal velocity ($v_{ex} \rightarrow v_{T_i}$), then the corresponding range of ion temperature required is $2\,\text{keV} < T_i < 4.5\,\text{keV}$. Thomson scattering measurements of T_i in the axial region ($r = 2$–3) of a 32 wire tungsten array have shown ion temperatures in the range $T_i = 2$–$3\,\text{keV}$,[17,18] consistent with the above estimate. A high ion temperature model is also consistent with the dominance of ion-ion collisions that was seen in the mean free path calculations. It is unlikely that the required ion heating can be explained by electron-thermal conduction from the axis, as this would require an electron temperature at least comparable to the ion temperature. Instead, it could be driven by the soft scattering of interpenetrating ion flows through the axis. The long mean free paths in these collisions mean that the ions are capable of significant penetration into the opposing streams, perhaps driving early heating. The decreasing mean free path, driven by increasing density, could potentially explain the observed decrease with time of the smoothing radius.

Further work is required to properly understand this process. In particular, further Thomson scattering measurements of the velocity distributions both in the streams and on axis are required. Although previous measurements[17,18] have shown a broad velocity distribution on axis, the scattering geometries used in these experiments mean that we cannot distinguish between axial and radial velocity contributions. This will be rectified in future work, allowing us to discriminate better between the various explanations proposed here.

VII. CONCLUSIONS

The formation of shock structures in the inter-wire regions was not observed in any of the tungsten wire array data collected during these experiments. Instead, the electron density profiles for the tungsten arrays were smoothly varying, with no apparent discontinuities. This contrasts with the data from similar aluminium array experiments,[10] where the electron density profiles were dominated by networks of oblique shock structures. The only reasonable explanation for this change in flow dynamics is that the change in wire material has led to a significant change in the collisional mean free paths associated with the interactions of the adjacent ablation streams. This result is important, as the grid-based magneto-hydrodynamic codes which are generally used to simulate wire array experiments treat the plasma as a fluid and therefore cannot model the effects of long collisional mean free paths.

The mean free paths for the interactions between adjacent ablation streams in both aluminium and tungsten arrays were calculated using Trubnikov's equations.[25] The results allowed us to explain the changes in collisional dynamics observed in aluminium wire arrays and to account for the absence of collisional features in the tungsten wire array data. Comparisons of the mean free path plots for aluminium and tungsten allowed us to estimate an upper limit on the $\bar{Z}$ of the tungsten ablation stream plasma of $\bar{Z} < 6$, corresponding to an electron temperature of $T_e \sim 6\,\text{eV}$ based on calculations using the LTE Saha rate solution. This temperature is slightly lower than that previously been suggested,[27] though perhaps this reflects the inaccuracy of a LTE solution under these plasma conditions. Thomson scattering measurements[17,18] have so far only placed an upper limit on the stream temperature, so clearly further measurements are required to explain these observations. The mean free path calculations indicate that as the electron density in the inter-stream region increases towards $10^{19}\,\text{cm}^{-3}$, we should expect to observe shock structure formation. It is hoped that we may see this transition in future experiments.

A modulation between the electron density in the ablation streams and in the inter-wire gaps was observed at large radius in all the data collected in these experiments; however, this modulation smoothed out rapidly as the streams approached the array axis, resulting in an azimuthally isotropic distribution within a certain radius of the axis. Observations of this process in both 8 and 32 wire arrays suggest that it is unlikely to simply be the result of the passive superposition of the density profiles of non-interacting ablation streams as they converge on axis. We suggested a number of possible mechanisms that might drive the smoothing process, such as transverse scattering of the streams, heating of the streams, and loss of magnetic confinement. The limits placed on the plasma by the absence of shocks means that if the streams are expanding thermally, then this expansion must be due to a high ion temperature. Any significant increase in electron temperature would be likely to trigger shock formation. It should be noted that a high ion temperature is consistent with previously published Thomson scattering results,[17,18] which show high ion temperatures near the axis, extending over a similar radius to that over which the smoothing process takes place.

Further work is required in order to properly understand which of these mechanisms is dominant. In particular, further Thomson scattering measurements of the transition region are required in order to separately measure the axial and radial flow velocity distributions.

The results of these experiments are important as they demonstrate some of the limitations of the modelling techniques currently used to simulate wire array z-pinches. Historically, magneto-hydrodynamic techniques have dominated simulation work in the field of wire array z-pinches; however, long mean free path dynamics cannot be reproduced using these approaches. The results presented in this paper demonstrate that long mean free path effects can be present in experiments for significant fractions of the experimental time. In order to reproduce the dynamics seen in these experiments we will need to apply particle-in-cell modeling techniques.

The results of these experiments are also interesting as they provide us with data about the behaviour of colliding plasma streams under the conditions of long mean free paths.

ACKNOWLEGMENTS

This work was supported by AWE, by EPSRC Grant No. EP/G001324/1 and by the NNSA under DOE

Cooperative Agreement Nos. DE-F03-02NA00057 and DE-SC-0001063.

APPENDIX: EQUATIONS USED TO CALCULATE MEAN FREE PATHS

The equations used to calculate the mean free paths in this paper were taken from the NRL plasma physics formulary[26] and were originally derived by Trubnikov.[25] The "slowing down" frequency, $\nu_s^{\alpha\backslash\beta}$, is defined as follows:

$$\frac{d\vec{v}_\alpha}{dt} = -\nu_s^{\alpha\backslash\beta}\vec{v}_\alpha. \tag{A1}$$

Here, α and β are labels for the test and scattering particles, respectively, $\vec{v}_\alpha$ is the initial test particle velocity, and $\nu_s^{\alpha\backslash\beta}$ is the exponential decay rate for $\vec{v}_\alpha$ due to the collisions of the α particles and the static field of thermal β particles. It is calculated using the following expression (in CGS):

$$\nu_s^{\alpha\backslash\beta} = \left(1+\frac{m_\alpha}{m_\beta}\right)\psi(x^{\alpha\backslash\beta})\lambda_{\alpha\beta}\left(\frac{4\pi e_\alpha^2 e_\beta^2 n_\beta}{m_\alpha^2 v_\alpha^3}\right). \tag{A2}$$

In this expression m_α and m_β are the masses of the two particles, $\psi(x^{\alpha\backslash\beta})$ is the velocity potential, $\lambda_{\alpha\beta}$ is the coulomb logarithm, e_α and e_β are the charges of the two particles, and n_β is the β particle number density. The mean free path for this process is defined as $l_0^{\alpha\backslash\beta} = \vec{v}_\alpha/\nu_0^{\alpha\backslash\beta}$:

$$l_0^{\alpha\backslash\beta} = \left(\left(1+\frac{m_\alpha}{m_\beta}\right)\psi(x^{\alpha\backslash\beta})\lambda_{\alpha\beta}\right)^{-1}\frac{(m_\alpha\vec{v}_\alpha^2/2)^2}{\pi e_\alpha^2 e_\beta^2 n_\beta}. \tag{A3}$$

This equation shows the basic scalings for $l_0^{\alpha\backslash\beta}$. It is directly proportional to n_β and scales quadratically with e_α, e_β and $(m_\alpha\vec{v}_\alpha^2/2)$ (the α particle kinetic energy).

For the calculations presented in this paper, $\lambda_{\alpha\beta}$ was found using the expressions in the NRL Plasma Physics Formulary.[26] In some cases, the calculated coulomb logarithm fell below unity. This is not physical and corresponds to situations where the Debye radius of the plasma becomes smaller than the minimum impact parameter. In these cases, the value of the coulomb logarithm was set to unity, which corresponds to the case where only large angle interactions are important. In most cases, the coulomb logarithm scales slowly and so it tends to be less important in terms of understanding the basic scalings of the collision length.

The velocity potential, $\psi(x^{\alpha\backslash\beta})$, is a normalised factor equal to the fraction of the β particle population whose speed is less than $|\vec{v}_\alpha|$. Contributions to $\nu_s^{\alpha\backslash\beta}$ from interactions with β particles travelling at speeds greater than $|\vec{v}_\alpha|$ cancel out, as these collisions act both to increase and decrease $\vec{v}_\alpha$. It is calculated by integrating over the Maxwell speed distribution function from 0 to v_α. The equations given in the literature[25,26] are

$$\psi(x^{\alpha\backslash\beta}) = \frac{2}{\sqrt{\pi}}\int_0^{x^{\alpha\backslash\beta}} dt t^{\frac{1}{2}}e^{-t}, \tag{A4}$$

$$x^{\alpha\backslash\beta} = \frac{m_\beta v_\alpha^2}{2kT_\beta}. \tag{A5}$$

Alternatively, these expressions may be rearranged into a more familiar form

$$\psi(v_\alpha, m_\beta, T_\beta) = 4\pi\left(\frac{m_\beta}{2\pi kT_\beta}\right)^{\frac{3}{2}}\int_0^{v_\alpha} v_\beta^2 e^{-\frac{m_\beta v_\beta^2}{2kT_\beta}}\, dv_\beta. \tag{A6}$$

[1]C. Deeney, T. J. Nash, R. B. Spielman, J. F. Seaman, J. S. McGurn, D. O. Jobe, M. F. Vargas, T. L. Gilliland, R. C. Mock, K. W. Struve, K. G. Whitney, P. E. Pulsifer, J. P. Apruzese, J. W. Thornhill, and J. Davis, Phys. Plasmas **5**, 2431 (1998).
[2]J. H. Hammer, M. Tabak, S. C. Wilks, J. D. Lindl, D. S. Bailey, P. W. Rambo, A. Toor, G. B. Zimmerman, and J. L. Porter, Phys. Plasmas **6**, 2129 (1999).
[3]M. Cuneo, R. Vesey, J. Porter, G. Bennett, D. Hanson, L. Ruggles, W. Simpson, G. Idzorek, W. Stygar, J. Hammer, J. Seamen, J. Torres, J. McGurn, and R. Green, Phys. Rev. Lett. **88**, 215004 (2002).
[4]J. E. Bailey, D. Cohen, G. A. Chandler, M. E. Cuneo, M. E. Foord, R. F. Heeter, D. Jobe, P. Lake, D. A. Liedahl, J. J. MacFarlane, T. J. Nash, D. Nielson, R. Smelser, and W. A. Stygar, J. Quant. Spectrosc. Radiat. Transf. **71**, 157 (2001).
[5]J. E. Bailey, G. A. Chandler, D. Cohen, M. E. Cuneo, M. E. Foord, R. F. Heeter, D. Jobe, P. W. Lake, J. J. MacFarlane, T. J. Nash, D. S. Nielson, R. Smelser, and J. Torres, Phys. Plasmas **9**, 2186 (2002).
[6]M. G. Haines, Plasma Phys. Controlled Fusion **53**, 093001 (2011).
[7]S. V. Lebedev, F. N. Beg, S. N. Bland, J. P. Chittenden, A. E. Dangor, M. G. Haines, K. H. Kwek, S. A. Pikuz, and T. A. Shelkovenko, Phys. Plasmas **8**, 3734 (2001).
[8]V. V. Aleksandrov, Plasma Phys. Rep. **27**, 89 (2001).
[9]M. E. Cuneo, E. M. Waisman, S. V. Lebedev, J. P. Chittenden, W. A. Stygar, G. A. Chandler, R. A. Vesey, E. P. Yu, T. J. Nash, D. E. Bliss, G. S. Sarkisov, T. C. Wagoner, G. R. Bennett, D. B. Sinars, J. L. Porter, W. W. Simpson, L. E. Ruggles, D. F. Wenger, C. J. Garasi, B. V. Oliver, R. A. Aragon, W. E. Fowler, M. C. Hettrick, G. C. Idzorek, D. Johnson, K. Keller, S. E. Lazier, J. S. McGurn, T. A. Mehlhorn, T. Moore, D. S. Nielsen, J. Pyle, S. Speas, K. W. Struve, and J. A. Torres, Phys. Rev. E **71**, 046406 (2005).
[10]G. F. Swadling, S. V. Lebedev, N. Niasse, J. P. Chittenden, G. N. Hall, F. Suzuki-Vidal, G. Burdiak, A. J. Harvey-Thompson, S. N. Bland, P. De Grouchy, E. Khoory, L. Pickworth, J. Skidmore, and L. Suttle, Phys. Plasmas **20**, 022705 (2013).
[11]C. Deeney, T. Nash, R. Spielman, J. Seaman, G. Chandler, K. Struve, J. Porter, W. Stygar, J. McGurn, D. Jobe, T. Gilliland, J. Torres, M. Vargas, L. Ruggles, S. Breeze, R. Mock, M. Douglas, D. Fehl, D. McDaniel, M. Matzen, D. Peterson, W. Matuska, N. Roderick, and J. MacFarlane, Phys. Rev. E **56**, 5945 (1997).
[12]R. B. Spielman, C. Deeney, G. A. Chandler, M. R. Douglas, D. L. Fehl, M. K. Matzen, D. H. McDaniel, T. J. Nash, J. L. Porter, T. W. L. Sanford, J. F. Seamen, W. A. Stygar, K. W. Struve, S. P. Breeze, J. S. McGurn, J. A. Torres, D. M. Zagar, T. L. Gilliland, D. O. Jobe, J. L. McKenney, R. C. Mock, M. Vargas, T. Wagoner, and D. L. Peterson, Phys. Plasmas **5**, 2105 (1998).
[13]D. B. Sinars, M. E. Cuneo, B. Jones, C. A. Coverdale, T. J. Nash, M. G. Mazarakis, J. L. Porter, C. Deeney, D. F. Wenger, R. G. Adams, E. P. Yu, D. E. Bliss, and G. S. Sarkisov, Phys. Plasmas **12**, 056303 (2005).
[14]D. B. Sinars, M. E. Cuneo, E. P. Yu, S. V. Lebedev, K. R. Cochrane, B. Jones, J. J. MacFarlane, T. A. Mehlhorn, J. L. Porter, and D. F. Wenger, Phys. Plasmas **13**, 042704 (2006).
[15]S. Bott, S. Lebedev, D. Ampleford, S. Bland, J. Chittenden, A. Ciardi, M. Haines, C. Jennings, M. Sherlock, G. Hall, J. Rapley, F. Beg, and J. Palmer, Phys. Rev. E **74**, 046403 (2006).
[16]M. Sherlock, J. P. Chittenden, S. V. Lebedev, and M. G. Haines, Phys. Plasmas **11**, 1609 (2004).
[17]A. J. Harvey-Thompson, S. V. Lebedev, S. Patankar, S. N. Bland, G. Burdiak, J. P. Chittenden, A. Colaitis, P. De Grouchy, H. W. Doyle, G. N. Hall, E. Khoory, M. Hohenberger, L. Pickworth, F. Suzuki-Vidal, R. A. Smith, J. Skidmore, L. Suttle, and G. F. Swadling, Phys. Rev. Lett. **108**, 145002 (2012).

[18]A. J. A. J. Harvey-Thompson, S. V. Lebedev, S. Patankar, S. N. Bland, G. Burdiak, J. P. Chittenden, A. Colaitis, P. De Grouchy, G. N. Hall, E. Khoory, M. Hohenberger, L. Pickworth, F. Suzuki-Vidal, R. A. Smith, J. Skidmore, L. Suttle, and G. F. Swadling, Phys. Plasmas **19**, 056303 (2012).
[19]I. H. Mitchell, J. M. Bayley, J. P. Chittenden, J. F. Worley, A. E. Dangor, M. G. Haines, and P. Choi, Rev. Sci. Instrum. **67**, 1533 (1996).
[20]G. F. Swadling, "An experimental investigation of the azimuthal structures formed during the ablation phase of wire array z-pinches," Ph.D. dissertation (Imperial College, 2012).
[21]S. Lebedev, F. Beg, S. Bland, J. Chittenden, A. Dangor, M. Haines, S. Pikuz, and T. Shelkovenko, Phys. Rev. Lett. **85**, 98 (2000).
[22]A. J. Harvey-Thompson, S. V. Lebedev, S. N. Bland, J. P. Chittenden, G. N. Hall, A. Marocchino, F. Suzuki-Vidal, S. C. Bott, J. B. A. Palmer, and C. Ning, Phys. Plasmas **16**, 022701 (2009).
[23]A. Ciardi, S. V. Lebedev, A. Frank, E. G. Blackman, J. P. Chittenden, C. J. Jennings, D. J. Ampleford, S. N. Bland, S. C. Bott, J. Rapley, G. N. Hall, F. A. Suzuki-Vidal, A. Marocchino, T. Lery, and C. Stehle, Phys. Plasmas **14**, 056501 (2007).
[24]J. P. Chittenden, S. V. Lebedev, C. A. Jennings, S. N. Bland, and A. Ciardi, Plasma Phys. Controlled Fusion **46**, B457 (2004).
[25]B. A. Trubnikov, Rev. Plasma Phys. **1**, 105 (1965).
[26]D. Book and J. D. Huba, *NRL Plasma Physics Formulary,* p. 31 (2002).
[27]J. P. Chittenden, S. V. Lebedev, B. V. Oliver, E. P. Yu, and M. E. Cuneo, Phys. Plasmas **11**, 1118 (2004).
[28]D. E. Post, R. V. Jensen, C. B. Tarter, W. H. Grasberger, and W. A. Lokke, At. Data Nucl. Data Tables **20**, 397 (1977).
[29]A. E. Kramida and J. Reader, At. Data Nucl. Data Tables **92**, 457 (2006).
[30]I. C. Blesener, J. B. Greenly, B. R. Kusse, K. S. Blesener, C. E. Seyler, and D. A. Hammer, Phys. Plasmas **19**, 022109 (2012).
[31]G. N. Hall, S. V. Lebedev, F. Suzuki-Vidal, G. Swadling, J. P. Chittenden, S. N. Bland, A. Harvey-Thompson, P. F. Knapp, I. C. Blesener, R. D. McBride, D. A. Chalenski, K. S. Blesener, J. B. Greenly, S. A. Pikuz, T. A. Shelkovenko, D. A. Hammer, and B. R. Kusse, Phys. Plasmas **20**, 022703 (2013).